View metadata, citation and similar papers at core.ac.uk

brought to you by CORE

provided by Apollo

A general approach for hysteresis-free, operationally stable metal halide perovskite field effect transistors

Satyaprasad P Senanayak[1], Mojtaba Abdi-Jalebi[1], Varun S. Kamboj[1], Remington Carey[1], Ravichandran Shivanna[1], Tian Tian[2,3], Guillaume Schweicher[1], Junzhan Wang[1], Nadja Giesbrecht[4], Daniele Di Nuzzo[1], Harvey E. Beere[1], Pablo Docampo[4,5], David A. Ritchie[1], David Fairen-Jimenez[2], Richard H. Friend[1] and Henning Sirringhaus[1*]

[1]Cavendish Laboratory, University of Cambridge, J.J. Thomson Avenue, CB3 0HE.

[2] Adsorption and Advanced Materials (AAM) Laboratory, Department of Chemical Engineering and Biotechnology, University of Cambridge, Philippa Fawcett Drive, Cambridge CB3 0AS, UK

[3]Department of Chemical Engineering, Imperial College London, South Kensington Campus, London SW7 2AZ, U.K.

[4]Department Chemie, Ludwig-Maximilians-Universität-München, Butenandtstr. München Germany.

[5]School of Electrical and Electronic Engineering, Newcastle University, Merz Court, Newcastle upon Tyne NE1 7RU, UK

Corresponding Author: hs220@cam.ac.uk

Abstract:

Lead halide perovskites are intensively researched and developed as semiconductor materials for high-performance solar cells and light-emitting diodes. However, for their electronic applications in field-effect transistors (FETs) there remain significant concerns despite sustained research efforts due to remaining operational instabilities and hysteresis effects linked to the ionic nature of these materials. Here, we investigate the mechanism behind these instabilities and demonstrate an effective route to suppress them and to realise high-performance perovskite FETs with low hysteresis, high threshold voltage stability ($\Delta V_T < 2V$ over 10 hours of continuous operation) and high mobility values > 1 cm^2/Vs at room temperature, which approaches the performance required for industrial applications in flexible electronic circuits and displays. We show that multiple cation incorporation using mixtures of small, strain-relieving cations such as Cs and cations such as Rb, which act as passivation / crystallisation modifying agents, is an effective strategy for reducing vacancy concentration and ion migration in perovskite FETs. Furthermore, we demonstrate that treatment of perovskite films with positive azeotrope solvents that act as Lewis bases (acids) enables a further reduction in defect density and significant improvement in performance and stability of n-type (p-type) perovskite devices.

Introduction

Hybrid organic-inorganic lead halide perovskites (like $CH_3NH_3PbI_3$; hereafter $MAPbI_3$) are a very promising and intensively researched class of semiconductor materials for next-generation high-performance optoelectronic devices that could potentially outperform conventional inorganic devices. Perovskite solar cells with certified power conversion efficiencies reaching up to 24.3% as well as light emitting diodes with external quantum efficiencies exceeding 20 %[1-3] have been demonstrated. Rapid progress has been enabled by the outstanding optoelectronic properties of lead halide perovskites, such as the long charge carrier diffusion length[4], low effective mass of the charge carriers[5] and clean band structure[6]. Consistent improvements of device performance and stability have been achieved by engineering of the interfaces[7, 8], developing perovskite composites with different semiconductors[9-11], use of carrier selective layers[12, 13] as well as the use of multi-cationic mixtures[14] and incorporation of low dimensional perovskite structures[15, 16]. Despite the remarkable, rapid advances in optoelectronics devices like photovoltaics, light emitting diodes[17] and optically pumped lasers[18] the fabrication of perovskite field effect transistors (FETs) has remained challenging[19]. This is because ion migration in these ionic materials causes a partial screening of the applied gate field, yielding reduced gate modulation of electronic charges at room temperature and reduced field-effect mobilities, $\mu_{FET,}$ of typically of 10^{-3}-10^{-4} cm^2/Vs in thin films or single crystals of $MAPbI_3$ [20-23]. For photovoltaic and light-emitting diodes ion migration also leads to a screening of the applied electric field in the semiconductor, but this does not significantly degrade the device performance as currents can be driven by diffusion through the semiconductor. The issue of ionic defect migration in $MAPbI_3$ perovskite FETs has been mitigated to some extent by operating the devices at low temperature wherein the ions are frozen or by using single crystals with low defect densities[24]. Usage of lead acetate precursor for fabricating $MAPbI_3$ thin films and modifications of the source-drain contacts with suitable interfacial layers has previously been shown to be effective to achieve reasonable FET characteristics from 100 K to 300 K with a μ_{FET} of 0.5 cm^2/Vs at room temperature[25]. In spite of these advances, $MAPbI_3$ FETs still exhibit non-ideal transistor characteristics with significant hysteresis and a high degree of bias stress-induced instability and large threshold voltage shifts upon continuous operation[25, 26]. Hence, for perovskite FETs to become more useful, both for fundamental transport studies as well as for potential applications, there is a need to develop approaches to improve their performance, long term operational stability and achieve hysteresis-free gate modulation.

Incorporation of multi-cation mixtures such as formamidinium (FA, $HC(NH_2)_2^+$) or Cs or Rb which either replace the methylammonium (MA) cation or act as passivation agents has been shown to increase stability and reduce hysteresis in photovoltaic devices[14, 27]. However, the molecular origin of stability in these multi-cationic perovskites remains incompletely understood. Here, we utilize FETs as a platform to investigate the molecular mechanism for the operational stability and hysteresis characteristics of multi-cation perovskites optoelectronic devices. Triple cation $Cs_x(MA_{0.17}FA_{0.83})_{1-x}Pb(Br_{0.17}I_{0.83})_3$ has been previously investigated and balanced ambipolar characteristics with field effect mobilities of 2 cm^2/Vs at room temperature were reported[28]; however, the hysteresis and stability were not studied. In the present work we perform a systematic investigation of performance and operational stability of multi-cation perovskite FETs and identify an effective strategy to suppress vacancy formation and ion migration in these materials through the use of Lewis base and acid treatments for n-type and p-type perovskite semiconductors, respectively. We demonstrate for the first time high performance, hysteresis-free perovskite FETs with mobilities > 1 cm^2/Vs and operational stability comparable to that of other established FETs technologies. Using electrical, spectroscopic and structural characterization we identify potential mechanisms for the suppression of ion migration in multi-cation compositions and acid/base treatments.

Results:

Optimization of Multi-cation perovskite FETs: The choice of the perovskite precursor material and the technique for solution deposition significantly affects the charge transport behaviour in perovskites. We showed previously that the use of $Pb(Ac)_2$ precursor improves the performance of bottom-contact, top-gate $MAPbI_3$ FETs [25], while devices fabricated with PbI_2 precursor exhibit much poorer performance in the same device architecture.[19, 20] We use here the same bottom-contact, top-gate FET architecture with gold source-drain contacts and a Cytop gate dielectric layer as in Ref. 31. Unfortunately, because of solubility constraints the use of $Pb(Ac)_2$ precursor severely limits the incorporation of multi-cation mixtures, such as FA, Cs or passivation agents (e.g. Rb, K) into $MAPbI_3$. Hence, we first sought to optimise the conventional PbI_2 precursor based $MAPbI_3$ perovskite thin film fabrication through the anti-solvent technique (**Method section** and supplementary section **S1**). In **Figure 1** we show the device characteristics of n-type, top-gate perovskite FETs fabricated with the anti-solvent method and different cation compositions. $MAPbI_3$ FETs made from PbI_2 precursor with anti-solvent (**Figure 1a**) exhibit at least an order of magnitude increase in the channel current

compared to devices fabricated without the anti-solvent technique (**Figure S1a**) and are comparable to devices fabricated with $Pb(Ac)_2$ precursor (**Figure S1c** & **d**). However, despite extensive optimisation the devices still exhibit significant hysteresis, evident in the transfer characteristics of **Figure 1a**, but particularly in the output characteristics at 300 K **(Figure S2)**, which bear the signature of ion migration under the action of the applied gate and source-drain (S-D) electric fields. Moreover, the output characteristics, particularly of devices with relatively small channel length (L = 20 µm), exhibit significant contact resistance, as evidenced by a suppression of the current at small source-drain voltages. Using the transfer line method in the linear regime of the output characteristics (forward sweep), the contact resistance was estimated to be as low as (400 ± 70) kΩ-cm at 300 K in the best devices, but we observed significant variations from batch to batch (**Figure S3**). To minimize the contact resistance, most devices discussed in the following were fabricated with a long channel length of 100 µm. Interestingly, $MAPbI_3$ FETs fabricated with L = 100 µm exhibit some improvement in the hysteretic performance at both 100 K and 300 K compared to devices fabricated with L = 20 µm (**Figure 1(b) & S2**).

Nevertheless despite extensive optimisation $MAPbI_3$ FETs retain significant hysteresis and non-idealities, that make them poorly suitable both for fundamental transport studies as well as applications and necessitate the exploration of more complex compositions. At 100 K, where ionic defect migration is negligible, the hysteresis can be attributed to the strong dipolar nature of the methylammonium cation (MA^+). As the effective electric field along the channel decreases with increased channel length, the polarization of the cation decreases and this manifests in the observed reduction in hysteresis at 100 K with longer channel length. Similar behaviour is observed when MA^+ is replaced by FA^+[29]. Bottom-contact, top-gate $FAPbI_3$ FETs exhibit near hysteresis-free transfer and output characteristics at 100 K, even for L = 20 µm (**Figure S4**). This is consistent with the measured dielectric constant $\varepsilon_r = Cd/\varepsilon_o A$ (where C is the capacitance, d is the film thickness, A is the area of the capacitor, and ε_o is the vacuum permittivity) which is estimated to be $\varepsilon_r \sim 27$ (at 100 kHz) for $MAPbI_3$ and decreases to 4.3 (at 100 kHz) for $FAPbI_3$ (**Figure S5**). Consequently, the expected dipole moment of the MA^+ and FA^+ cations at room temperature, estimated using the Kirkwood-Fröhlich formalism for polar, orientationally disordered solids, are 1.94 D and 0.45 D respectively (**Supporting Section S2**)[30-32].

Unfortunately, the hysteresis-free characteristics of $FAPbI_3$ are not retained to room temperature and also the magnitude of the transistor current I_{ds} is lower by up to two orders

of magnitude for $FAPbI_3$ than for $MAPbI_3$ at 300K (**Figure S6**). This can be attributed to the co-existence of a small fraction (~ 5.7 %) of the non-perovskite δ-$FAPbI_3$ phase along with the perovskite α-$FAPbI_3$ phase, which is evident in the XRD patterns (**Figure S7**) and the shape of the optical absorption edge measured by photothermal deflection spectroscopy (PDS) (**Figure S8**)[33]. The issue of the non-perovskite yellow phase can be mitigated by introduction of mixed cation compositions of FA^+, MA^+, Cs^+ while maintaining iodide as the halide ion (**Supporting Section S4**)[27, 34]. We undertook an optimization of composition and identified $FA_{0.2}MA_{0.8}PbI_3$ (referred to as $FAMAPbI_3$ hereafter) and $Cs_{0.05}FA_{0.17}MA_{0.78}PbI_3$ ($CsFAMAPbI_3$) as optimized compositions which exhibit nearly hysteresis-free transfer characteristics at 300 K with a μ_{FET} ~ (0.1 ± 0.03) cm^2/Vs and ~ (0.3 ± 0.05) cm^2/Vs, respectively (**Figure 1c** & **Supporting Section S5**) which is comparable to the best $MAPbI_3$ devices with μ_{FET} ~ 0.5 cm^2/Vs. FETs with L = 100 μm fabricated from $FAMAPbI_3$ and $CsFAMAPbI_3$ also exhibited significant improvement in output characteristics measured at 300 K with well-defined linear and saturation regimes (**Figure 1d**). We also fabricated devices with more complex compositions, such as $Cs_{0.05}FA_{0.78}MA_{0.17}Pb(I_{0.78}Br_{0.17})_3$, for which high solar cell efficiencies have previously been reported[27]; these exhibited rather lower μ_{FET} ~ 0.003 cm^2/Vs (**Figure S13b**). To further enhance FET performance we also explored Rb passivation by adding RbI solution into the $CsFAMAPbI_3$ precursor solution in varying composition (1%, 5%, 10%). Interestingly, upon addition of RbI we observed an increase in the channel current and μ_{FET} reached a value of ~ 0.8 cm^2/Vs in best devices for a 5% concentration of Rb in solution (referred as $RbCsFAMAPbI_3$ hereafter) (**Figure 1e**). Further increasing the Rb concentration to 10 %, μ_{FET} significantly drops down to ~ 0.001 cm^2/Vs (**Figure S14a**) which is consistent with the observation of a phase segregated, Rb-based non-perovskite phase both in XRD and SEM (**Supporting Section S4**)[35] Similar enhancement in charge carrier mobility upon addition of Rb to $CsFAMAPbI_3$ has also been observed through microwave conductivity and time of flight measurements[36]. Surprisingly, the output characteristics measured on Rb passivated devices exhibited even cleaner, hysteresis-free output characteristics (**Figure 1f**). We also explored potassium passivation for $CsFAMAPbI_3$ which has been shown to inhibit ionic migration and remove hysteresis in solar cells but this resulted poor μ_{FET} ~ 10^{-4} cm^2/Vs and loss of gate modulation upon increasing the K composition to 10 %. We attribute this behaviour to the formation of a segregated, non-conducting KI ionic solid phase which screens the gate potential (**Figure S14b**)[37]. Nevertheless, from these wide compositional variation we understand that even a small variation of 1-2 % of specific cations is enough to drastically degrade the FET performance.

This behaviour can be related to a number of factors like the the propensity to phase segregation as well as disorder energetics and the overall stability of the crystal structure (as shown in the later sections).

Ionic defect dynamics: To directly probe ion migration at 300 K in these devices, we monitored the temporal variation of the channel current and the optical properties of the channel while the perovskite FET is operated continuously in the trans-diode mode ($V_d = V_g = 60$ V) (**Figure 2**). The $I_{ds}(t)$ characteristics of $MAPbI_3$ devices (**Figure 2a**) exhibit a complex behaviour for the first 10's of seconds that depends on channel length, but at later times a rise in the current is observed, which sets in the earlier for devices with shorter channel lengths. This rise in the current is attributed to lateral ionic defect migration resulting in healing of iodine vacancies and/or decrease in the contact resistance when ions start to accumulate at the metal-semiconductor interface[38, 39]. After prolonged biasing (>100-1000s) the current is observed to decrease; this potentially reflects processes involving electrochemical degradation of the electrodes. The characteristic time scale for ion/defect migration can be estimated from the intersection of linear fits of the early time behaviour and the current rise (as indicated in **Figure 2a**). The characteristic time scale for the onset of ionic migration (τ_c) is observed to change from 8 s for FETs with L = 20 μm to 38 s for FETs with L = 100 μm (**Figure 2b**). Using a simplistic time of flight estimation the mobility of the ions can be estimated as 5×10^{-7} cm^2/Vs, which is comparable to the reported values for iodine migration in $MAPbI_3$[39, 40]. This behaviour correlates well with the observed improved performance of long channel devices and also the observation that the extracted temperature dependent mobility $\mu_{FET}(T)$ decreases more rapidly with increasing temperature for small L (**Figure S15**). In $FAMAPbI_3$ and $CsFAMAPbI_3$ devices τ_c increases to 72 s and 226 s and for Rb-passivated $CsFAMAPbI_3$ the current remains stable for 10^3 seconds indicating a much-improved stability towards ionic/defect migration by addition of Rb (**Figure 2c**). This is fully consistent with the absence of hysteresis in the FET characteristics.

Photoluminescence Mapping of Ionic Defects: We also visualized iodine migration by performing photo-luminescence (PL) mapping (in nitrogen atmosphere) under bias on lateral devices (L ~ 20 μm). Unbiased devices exhibited uniform PL intensity profile throughout the channel (**Figure 2d**). Devices were then poled at $V_d = 60$ V for 180 seconds and PL mapping was performed over the same area. Upon biasing, the PL profiles of $MAPbI_3$ devices exhibit an approximately exponential decay, with the positive electrode exhibiting a lower PL

intensity and the negative electrode exhibiting a higher PL intensity(**Figure 2d-f**). This trend is similar to the observation where photo induced brightening occurs when iodine is depleted and decrease in PL intensity is observed upon accumulation of iodine defect[39, 41]. This has been well studied by exposing perovskite films to laser illumination[41], voltage bias[39] and I_2 vapours. Upon increasing the channel length the characteristic decay length of the PL (after 180 seconds of biasing) away from the negative electrode decreases (**Figure 2e** & **f**) from 0.3 x L for 10 μm devices to 11.5 x L for 100 μm devices. Devices fabricated with $RbCsFAMAPbI_3$ thin films exhibited negligible variation in the PL profile even after biasing (at V_d = 60 V for 180 seconds) providing further evidence for the much reduced ion migration upon Rb passivation (**Figure 2g** & **h**).

To understand the beneficial effect of multi-cation composition on ion migration, we estimated the vacancy formation energy (H_f), which is directly proportional to the latent heat of fusion or decomposition of the crystal (L_f), i.e., $H_f = (L_f \times M)/C$ where M is the molar mass of the material and C is a constant which is dependent on the crystal structure of the material[42]. We estimated the heat of fusion/melting for the perovskite thin films from dynamic scanning calorimetry. A clear phase transition possibly due to the volatilization of cations and/or residual iodine which corresponds to the decomposition of the perovskite crystal structure is observed in all the perovskite thin films and the decomposition temperature was observed to increase from 191 °C for $MAPbI_3$ to 243 °C for $RbCsFAMAPbI_3$ thin films (**Figure S16**). Correspondingly, the enthalpy of fusion/decomposition increases from 11 J/g in $MAPbI_3$ thin films to ~ 88 J/g in $RbCsFAMAPbI_3$ thin films (**Table 1** in **Supporting Information**). After correcting for the molar mass of the perovskites and assuming the same tetragonal crystal structure, H_f is estimated to increase by a factor of eight for $RbCsFAMAPbI_3$ compared to $MAPbI_3$, suggesting that the vacancy concentration is indeed expected to be lower in the former.

Magnetic Signatures of Ionic Defects in Perovskites: To obtain a spectroscopic signature of the defects involved in ion migration we performed electron paramagnetic resonance (EPR) on solid crystalline samples. At room temperature no EPR signal was detected on any of the compositions, but upon cooling the samples to a temperature < 40 K a well-defined EPR resonance was observed (**Figure 3a**). It has a simple, narrow lineshape and cannot be attributed to the MA^+ cation which is expected to exhibit a multiple peak shape due to cationic radicals and the interaction of the un-paired electrons with H and N nuclei. Similarly,

any iodine related centres with a nuclear spin of 5/2 are expected to exhibit a hyperfine splitting with six lines[43, 44]. Hence, the observed EPR signal can only be attributed to the paramagnetic states of Pb^{+} or Pb^{3+}. The observation of an isotropic signal with a g ~ 2.0007 points to $6s^1$ electrons of Pb^{3+} as the origin of the EPR since Pb^{+} would be expected to exhibit strongly axial g-tensors with a g value between 1 – 1.7[43, 44]. Based on the EPR spectra, the spin density is estimated to be 1.1×10^{14} cm^{-3} for $MAPbI_3$ samples; this decreases to 5.2×10^{12} cm^{-3} for $RbCsFAMAPbI_3$ (details in **Methods Section**). However, it is important to note that the spin density estimated from EPR is too low to directly cause device hysteresis, as this would require the thickness integrated spin density in our typically 150-200 nm thick perovskite films to be comparable to the FET induced charge density, which is on the order of 10^{11}-10^{12} cm^{-2}. This suggests that not all defects causing hysteresis are EPR active. One plausible explanation that has been put forward in the literature is that the Pb^{3+} defects are due to substitution of lattice iodine by oxygen[44]. This could explain the observed reduction in EPR spin density for the multiple cation compositions, as the density of such oxygen related defects is likely to be the smaller the lower the iodine vacancy concentration. We also measured the temperature dependence of the magnetic susceptibility (χ) using a SQUID magnetometer (**Supporting Section S8, Figure S17**). From these measurements we estimate the spin concentration to be 2.1×10^{18} cm^{-3} for $MAPbI_3$ samples which decreases by an order of magnitude to 2×10^{17} cm^{-3} for $RbCsFAMAPbI_3$; such spin concentrations are large enough to be directly involved in device hysteresis. This observation provide evidence for a reduction of defect density in multiple cation systems; it is also consistent with our interpretation that the Pb^{3+} defects observed in EPR are merely a fingerprint of iodine vacancies, i.e., originate from vacancy sites that are occupied by oxygen.

Probing the Lattice Strain in Perovskite with THz spectroscopy: To investigate the charge carrier dynamics and elucidate further the origin of the improved hysteresis we performed broadband terahertz (THz) time-domain spectroscopy on operating FETs and observed the variation of specific phonon bands under bias. For these measurements we used a bottom-gate, bottom-contact FET architecture on moderately doped Si/SiO_2 wafers. This device architecture was preferred to allow probing of the channel in the transmission geometry since conducting metals used in the top gate geometry completely absorb the terahertz radiation and do not permit probing the channel region (details in **Supporting Section S9** and **Methods Section**). Broadband THz spectroscopy on perovskite thin films exhibits three prominent peaks close to 1 THz, 1.8 THz and 2.8 THz that can be attributed to

Pb-I octahedron cage vibrations (details in **Supporting Section S9**)[44-46]. Upon biasing $MAPbI_3$ devices in trans-diode mode (V_d = 60 V, V_g = 60 V) we observe a broadening of ($\Delta\omega$) ~ 0.08 THz for the lowest energy 1 THz phonon mode which is related to octahedron distortion involving a change in I-Pb-I bond angle (**Figure 3b-d** and **S18**). Interestingly, this broadening of the phonon mode decreases upon substituting with multi-cationic mixture and is negligible for devices fabricated with $CsFAMAPbI_3$ and $RbCsFAMAPbI_3$ (**Figure 3b,c** and **S19**). The phonon mode at 2.8 THz which governs the coupling between the A-cation and the Pb-I octahedron cage exhibits a sharpening of around 10 GHz under bias for $MAPbI_3$ devices; this can be attributed to a decrease in entropy of the MA^+ cation upon biasing (**Figure S21a**). No such variation is observed in the phonon mode at 2.6 THz under bias in $FAMAPbI_3$ (**Figure S21b**). A possible interpretation of the bias induced broadening at 1 THz is that it reflects the significant strain in the $MAPbI_3$ lattice, that could be released when the injected electrons polarize the I-Pb bond[46]. Since the energy levels of these perovskites originate from the Pb-6p and I-5p orbital, distortion of the Pb-I octahedron cage under bias modifies the energy landscape for charge transport and could also be a factor in the hysteretic characteristics. Lattice strain originates due to ionic size mismatch between the A-cation and the lead halide cage, and strain relaxation occurs through vacancy formation[47]. Through the incorporation of smaller cations such as Cs into the lattice the strain is expected to be significantly reduced[48] making the lattice more stable and less susceptible to distortions upon charge injection. The beneficial effect of Rb is unlikely to be directly related to such strain relaxation as Rb has been found not to be directly incorporated into the perovskite lattice, it could be due to changes in crystallization kinetics and improved crystalline quality instead.

Moisture adsorption in perovskites: Despite the observed enhancement in FET performance with the utilization of Rb-passivated $CsFAMAPbI_3$ perovskite the output characteristics are still not completely ideal and exhibit injection limited characteristics (**Figure 1f**). Moreover, the best estimated μ_{FET} ~ 0.8 cm^2/Vs is lower than the maximum mobility values that could theoretically be achievable in this class of materials suggesting room for further improvement[30]. Hence, we considered the role of extrinsic impurities like water and/or oxygen which are well known to severely degrade charge transport properties in n-type organic semiconductors[49-52]. Adsorbed water is ubiquitous in perovskite FET device fabrication due to the hygroscopic nature of the perovskite precursor and solvents and residual moisture/oxygen in the substrate, dielectric layer and the nitrogen glovebox used for film processing and device testing[53]. These water molecules get incorporated into pores in the

thin films or at grain boundaries and could act as trap centre for electron charge transport[49]. Typical transfer characteristics obtained on perovskite FETs upon exposure to ambient moisture condition are shown in **Figure S22a**. In order to quantify the porosity of the perovskite films, N_2 adsorption isotherms at 77 K were measured on perovskite thin films by performing suitable sample degassing (details in **Method Section**) without any sample degradation. All the samples exhibit Type III isotherms indicating weak adsorbent-adsorbate interaction and absence of any microporosity, but the presence of small amount of meso-pores. N_2 adsorption isotherms exhibited the highest Brunauer–Emmett–Teller (BET) surface area for $MAPbI_3$ thin films which decreases by half for $RbCsFAMAPbI_3$ (**Figure S24 a,b**). We also observed a comparable weight loss which can be attributed to a number of factors like water[54], residual solvent and/or methyl ammonium cation evaporation in TGA measurements at T = 100 °C; $MAPbI_3$ thin films exhibited a weight loss of 4-5 % while $RbCsFAMAPbI_3$ thin films exhibited a much smaller weight loss of only 1%. This is consistent with a reduced mesoporosity and BET surface area in $RbCsFAMAPbI_3$ and therefore a reduced susceptibility to water adsorption (**Figure S24d**). To study the performance of perovskite films in the strict absence of water, we placed a bottom gate bottom contact $MAPbI_3$ device near a strong desiccant cobalt (II) chloride. FETs exposed to $CoCl_2$ exhibited a significant increase in performance (**Figure 4a**) with higher ON current and decreased sub-threshold swing from 16 V/dec to 11 V/dec indicating a decrease in trap density.

Azeotropic Solvent treatment on Perovskite: An alternative technique to reduce the water content in the films, that has recently been found to be very effective for organic semiconductors[55], is to wash the top surface of the perovskite film with an orthogonal solvent which forms a positive azeotrope with water[56]. Azeotropes are formed when two or more liquids form a constant boiling mixture with a boiling point lower (higher) than that of the constituent liquid, which is referred to as a positive (negative) azeotrope. Before spin coating the top dielectric layer and the gate electrode we treated $MAPbI_3$ films with the following solvents, that form positive azeotropes with water: diethylether, methyl acetate, ethyl acetate, pyridine, 1,3,5-tri-nitrobenzene, 1,3,5 tri-bromobenzene. We also investigated the zeotropic solvents, fomblin, and acetic acid, that do not suppress the boiling point of water (**Table 2** in **Supporting Information**)[57]. Devices treated with diethylether, which exhibits the lowest boiling point azeotropic mixture of 34 °C, exhibited an increase in I_{ds} by two orders of magnitude (**Figure 4b**) whereas $MAPbI_3$ devices treated with pyridine with an azeotropic

boiling point of 92 °C exhibited no improvement in ON current (**Figure 4c**)[56]. We observe a clear correlation between the boiling point lowering of the water-solvent azeotropic mixture and the enhancement in the transistor ON current. The positive azeotrope treatment also leads to a positive shift in the FET turn-on voltage (**Figure 4b**) and a decrease in the subthreshold swing (**Figure S25**); correspondingly, the estimated trap density decreases from 10^{13} $cm^{-2}eV^{-1}$ to 10^{12} $cm^{-2}eV^{-1}$ (details in Supporting Section S11)[58, 59]. This suggests that the positive azeotrope treatment effectively removes water from the films.

However, water removal is not the only factor that governs the efficacy of such solvent treatments. A second key factor appears to be whether the solvent acts a Lewis acid or a Lewis base: $MAPbI_3$ devices treated with 1,3,5-tri-nitrobenzene, which has an azeotropic boiling mixture of 98 °C but acts as Lewis acid, exhibited a complete loss in gate modulation (**Figure S27**). In contrast devices treated with zeotropic acetic acid which acts as a Lewis base due to the oxygen electron lone pair in the acetate group exhibited rather similar ON current as pristine samples. In fact all the positive azeotrope that were found very effective are able to form Lewis base pairs with unsaturated Pb centres. Unfortunately, it was not possible to find a solvent which forms a negative azeotrope with water, acts a Lewis base and has a solubility that is sufficiently orthogonal to the perovskite.

A potential explanation for the efficacy of positive azeotrope, Lewis base treatments in improving the performance of these n-type perovskite films is that the process of perovskite film fabrication results in formation of electron trap sites linked to water/oxygen incorporation and potentially to over-co-ordinated Pb^{3+} species with a net positive charge. This creates a favourable condition for co-ordination or formation of a dative bond with electron-rich Lewis base solvent molecules which passivates the over-co-ordination by donating un-paired electrons [56]. To investigate this mechanism we performed solvent treatment on solid samples of $MAPbI_3$ and counted the number of free spins attributed to the Pb^{3+} ions both before and after solvent treatment. Upon treatment with a Lewis base solvent (details in **Methods Section**), the number of paramagnetic Pb^{3+} ions detected in EPR approximately halves to 7×10^{13} cm^{-3} and the overall paramagnetic defect density extracted from the magnetic susceptibility decreases to 1.3×10^{18} cm^{-3} (**Figure 3a and S17**). In the PL mapping across the lateral channel the treated films exhibited a weaker decay constant and significantly less iodine defect migration than untreated $MAPbI_3$ (**Figure 2g-h**). When $MAPbI_3$ films were dipped in methyl acetate as the Lewis Base for 24 hours and monitored

by XRD at regular intervals we also observed a change in lattice constant from 6.18 Å to 6.22 Å, which could indicate incorporation of the solvent into the crystal lattice or potentially relaxation of strain due to a reduced defect/vacancy (**Figure 4d**). No difference in the XRD pattern was obtained when the perovskite layer was treated only for short times in the same way as used for device fabrication (details in **Method Section**) indicating that for short exposure the effect is limited to a thin surface layer.

We performed such Lewis base, positive azeotrope treatments also on Rb-passivated $CsFAMAPbI_3$ based perovskite FETs and this resulted in improvement in the injection limited behaviour in the output characteristics (**Figure 5a**) and observation of a clean hysteresis-free output and transfer characteristics with a μ_{FET} reaching values of 1.2 cm^2/Vs (**Figure 5b**). Details of the μ_{FET} versus V_g is shown in Figure S26a and the histogram distribution of mobility is depicted in figure S26b. We further confirmed the operational stability of the perovskite FETs through voltage bias stress measurements. The devices were operated continuously for 10 hours in a trans-diode mode ($V_d = V_g = 60$ V) and the shift in threshold voltage (V_{th}) was monitored. We observe a pronounced improvement in the threshold voltage shift (ΔV_t) stability. Devices fabricated with pristine $MAPbI_3$ thin films exhibited $\Delta V_t \sim 10$ V after 10 hours of continuous operation while devices fabricated with solvent treated $RbCsFAMAPbI_3$ exhibit only $\Delta V_t \sim 2$ V after the same stress (**Figure 5c**). Subsequently, the transistors recover to their original characteristics upon removal of bias stress. This degree of threshold voltage stability (~3 % of the operating voltage) has never been demonstrated for a perovskite FETs and is approaching that of other transistor technologies, such as organic or amorphous silicon transistors.

Optimization of p-type Perovskite FETs: Inspired by these results, we investigated also p-type perovskites and aimed to translate the strategies learnt from the n-type perovskite FETs to p-type devices. Demonstration of gate modulation in thin films of p-type perovskite FETs has hitherto been difficult at room temperature. We were able to observe room temperature p-type transfer characteristics in $FA_{0.8}MA_{0.2}PbBr_3$ ($FAMAPbBr_3$) with a mobility $\mu_{FET} \sim 0.005$ cm^2/Vs (**Supplementary Section S12**). When using cationic compositions comprising Cs with bromide perovskites, however, no gate modulation (**Figure S30c**) was observed at room temperature. This could be attributed to the stronger propensity to CsBr formation resulting in a phase segregated non-perovskite phase in the material[35]. When $FAMAPbBr_3$ FETs were treated with Lewis base solvents (like diethyl ether or methyl acetate) we observed

degradation of the charge transport characteristics (**Figure S29**). However, when the p-type $FAMAPbBr_3$ layer was treated with the Lewis acid 1,3,5 tri-bromobenzene instead we observed an improvement in the transistor performance and a clean hysteresis-free p-type transistor performance with μ_{FET} ~ 0.02 cm^2/Vs (**Figure 5d and S30b**). This suggests that in the p-type devices there is a density of hole traps caused by structural defects and vacancies in the perovskite or by impurities such as water that can be eliminated/passivated by an electron withdrawing Lewis acid treatment.

Optimization of bottom gated perovskite structure: We also explored the optimisation of device performance through acid/base treatments in bottom-gate device architectures. However, the solvent-based Lewis acid or base treatments discussed above, which worked well for bottom-contact, top-gate perovskite FETs, did not have any effect on the performance of bottom-contact, bottom-gate devices on Si/SiO_2 wafers due to the fact that the effect of solvent effect is mainly limited to the surface and does not significantly affect the buried interface between the perovskite and the SiO_2 gate dielectric (**Figure S31**). We explored instead the effect of halides such as F^- and I^- and divalent additives like Zn^{2+}, Cd^{2+} which behave as soft Lewis bases and acids. We introduced F^- ions at the interface by spin coating 1-butyl-3-methylimidazolium tetrafluoroborate based ionic liquid (IL). I^- ions were introduced through NH_3-terminated self-assembled monolayers (3-Aminopropyl)-tri-ethoxysilane which were treated with HI to obtain iodide termination (details in **Method Section**). $RbCsFAMAPbI_3$ devices fabricated on IL or SAM treated interfaces exhibited enhanced performance (**Figure 5e** and **Figure S32**) and μ_{FET} increased from ~ 0.1 cm^2/Vs to up to 0.3 cm^2/Vs. However, addition of divalent cations like ZnI_2 (details in **Method Section**) which are Lewis Acids into n-type $RbCsFAMAPbI_3$ led to a decrease in the ON current and a minor increase in the OFF current with an overall μ_{FET} of 10^{-3} cm^2/Vs (**Figure S33**). On the other hand when divalent cationic salts like $ZnBr_2$ or ZnI_2 (in varying composition) were added into p-type $FAMAPbBr_3$ and $FA_{0.85}MA_{0.15}(Pb_{0.5}Sn_{0.5})I_3$ (referred as $FAMA(PbSn)I_3$ hereafter), respectively, we observed significant enhancement in the channel current by an order of magnitude and μ_{FET} increased from 0.002 cm^2/Vs to 0.007 cm^2/Vs with the best μ_{FET} was observed for samples passivated with 5 % ZnI_2 (**Figure S34-35**). The bias stress instability in the bottom-gated $RbCsFAMAPbI_3$ devices also decreased from ΔV_{th} ~ -17 V to ~ -5V upon introduction of Lewis base I^- at the interface (**Figure S36**). We also evaluated mixed Pb-Sn bottom-gate perovskite FETs based on $FAMA(PbSn)I_3$ that also exhibited p-

type characteristics and showed improved bias stress stability from ΔV_{th} ~ 14 V to ~ 9 V upon passivation with Lewis acid based ZnI salts (**Figure S36**).

Finally, to demonstrate that stable perovskite films can be obtained by low-temperature processing we fabricated bottom-contact, top-gate perovskite transistors on poly(ethylene terephthalate) (PET) substrates. $RbCsFAMAPbI_3$ devices on PET exhibited similar hysteresis-free characteristics as on glass substrates, however with a marginal drop in the μ_{FET} ~ 0.5 cm^2/Vs. This may be due to the difference in the surface energy or roughness between glass and PET substrates **(figure 5f)**.

Discussion: Detailed investigation of FET performance among different compositions of perovskite materials fabricated from different composition indicates the low tolerance of perovskite materials to small variations in precursor stoichiometry. Despite major differences in the operation of photovoltaic and FETs, it is interesting to observe that only certain compositions exhibit excellent performance. Moreover, a small variation of about 0.05 % variation from the high performing composition is enough to significantly impact the overall performance as well as stability of optoelectronic devices[60]. This can be related to the formation of phase-pure perovskite, stable lattice structure with low degree of disorder.

Conclusion: Our work demonstrates a practical strategy for obtaining operationally stable, hysteresis-free perovskite transistors with performance approaching the level required for large area integrated electronic applications. By incorporating appropriate small inorganic cations, such as Cs, into the perovskite lattice and using passivation agents, such as Rb, we have been able to reduce ionic defect migration at room temperature to a level at which it does no longer manifest itself in significant device hysteresis. Furthermore with solvent treatments based on Lewis base and Lewis acid azeotropes we achieve further optimisation in device performance and stability for n-type and p-type operation, respectively. Our work opens up the possibility of utilizing these novel materials for application prospects in large area electronics, for example, as n-type devices in complementary circuits with high mobility p-type organic semiconductors, and makes FET architectures a more powerful tool for investigating the charge transport physics of perovskite semiconductors. Moreover, the understanding of the instability and strategies evolved would inspire analogous techniques for improving the efficiency and stability of perovskite LEDs and solar cells.

Materials and Methods:

Perovskite film preparation: CH_3NH_3I was synthesized according to a previously reported procedure[25]. Absolute ethanol (100 ml) was used to dilute 24 ml of methylamine solution (33% in ethanol) in a 250-ml round bottom flask, followed by the addition of 10 ml of aqueous solution of hydriodic acid (57 weight %) under constant stirring. After 1 hour of reaction time at room temperature, a rotary evaporator was used to remove the solvents from the reaction mixture. The white solid residual was then washed using dry diethyl ether and recrystallized from ethanol to obtain methylammonium iodide crystals (CH_3NH_3I). Other precursor materials which include Lead(II) acetate trihydrate, Cesium Iodide, Rubidium Iodide, Cesium Bromide, Rubidium Bromide, Tin Iodide were used as obtained from Sigma Aldrich. Similarly, precursor materials Formamidinium Iodide, Formamidinium Bromide, Methyl ammonium bromide were obtained from GreatCell Solar Inc and used as received. The precursor solutions for the perovskite material were obtained by mixing the respective precursor materials in DMF at 0.75 M concentration to obtain $MAPbI_3$, $FA_{0.2}MA_{0.8}PbI_3$, $FA_{0.05}MA_{0.95}PbI_3$, $FA_{0.1}MA_{0.9}PbI_3$, $FA_{0.8}MA_{0.2}PbBr_3$ and in DMF:DMSO (4:1) at 0.75 M concentration for $Cs_{0.05}FA_{0.17}MA_{0.78}PbI_3$ and $Rb_{0.05}Cs_{0.05}FA_{0.15}MA_{0.75}PbI_3$, $Cs_{0.05}FA_{0.17}MA_{0.78}PbBr_3$, $FA_{0.85}MA_{0.15}(Pb_{0.5}Sn_{0.5})I_3$. Freshly prepared precursor solutions were spin coated using the anti-solvent technique at 5000 rpm for 3 minutes and annealed at 100 ^{0}C for 30 minutes. The above compositions reflect the concentration of the different cations/anions in solution. This is not meant to suggest that they are necessarily incorporated into the solid perovskite lattice in the same proportions; it is known, for example, that Rb is not incorporated into the perovskite lattice, but merely acts to modify the crystallization kinetics and potentially passivates defects at grain boundaries.

FET fabrication and measurement: Bottom-contact, top-gate field-effect transistors were fabricated on Cr/Au (3 nm:22 nm) source-drain electrodes which were evaporated and patterned photo-lithographically on pre-cleaned, plasma-treated glass substrates. This was followed by the deposition of the perovskite layer as described above. For the solvent treatment of the perovskite layer, an orthogonal solvent is introduced on top of the perovskite layer for 2 minutes covering the surface of the perovskite film. This was followed by spinning the solvents off the perovskite film at 2000 rpm for 60 seconds and annealing the solvent treated perovskite films at 100 ^{0}C for 30 minutes. A Cytop dielectric layer of ~500 nm thickness was then spin-coated over the perovskite film and annealed at 90°C for 20 min. The devices were then completed by evaporating the Au gate electrode (25 nm) through a shadow mask. For flexible devices, this method was adopted on PET substrates. For bottom-

contact, bottom-gate devices lithographically patterned source-drain electrodes were obtained on n^{++}-type Si (100) wafers (resistivity < 0.005 Ω cm, Active Business Company GmbH) with 300 nm of SiO_2 layer (capacitance C_i = 11.5 $nFcm^{-2}$). All the transfer characteristics were measured in pulsed mode, and the output characteristics were measured in continuous mode using an Agilent 4155B parameter analyzer. Note that in the pulsed mode of operation, for the transfer measurement V_g, was applied over a short impulse of 0.5 ms. In the continuous mode of operation, the voltages were applied continuously during the scan. To ensure reproducibility of the device and avoid any degradation of the interface, all the steps for device fabrication were performed in a nitrogen filled glovebox.

SAM treatment: (3-Aminopropyl)triethoxysilane (APTES) was purchased from Aldrich and used as received (storage under a N_2 atmosphere). Si/SiO_2 wafers were fully immersed for 45 min in a 4mM APTES solution in anhydrous toluene. Following the treatment, wafers were rinsed by toluene, acetone, and isopropanol and then sonicated for 5 min in fresh toluene. The NH_2-SAM is converted to NH_3I-SAM by treating the wafers in a 1mM solution of HI in water for 1 minute and then annealing at 100°C for 10 mins. Devices were then fabricated on these SAM treated Si/SiO_2 substrates.

Ionic Layer: 0.1 wt% of 1-Butyl-3-Methylimidazolium tetrafluoroborate was dissolved in methanol solution and spin coated at 2000 rpm for 60 seconds followed by annealing at 100°C for 30 minutes.

ZnI_2 and CdI_2: For introducing Group 12 salts ZnI_2 and CdI_2 were mixed with FAI in 1:1 mixture and then added with varied composition into the respective perovskite mixture.

Bias stress measurements: Considering the fact that defect migration due to high operating voltage is a primary cause of operational instability in perovskite transistors, voltage bias stress measurements were performed while the transistor was operated continuously in a trans-diode mode at V_d = V_g = 60 V. Transfer curves were measured every one hour and the shift in the threshold voltage was extracted as a measure of operational stability.

THz absorption spectroscopy: Broadband terahertz time-domain spectroscopy was carried out with a Tera K15-T-Light MENLO system on back-gated, bottom-contact perovskite transistors. The measurement involved pulses from a 30-mW pump laser of 90 fs duration at 1560 nm (repetition rate of 100 MHz) which is split into two paths: (i) a component focused down to a 40 µm spot onto the THz emitter, resulting in a broadband THz emission with a

spot size of ~1 mm, and (ii) a component through the delay stage for coherent THz detection. For the back gated transistor, mildly doped Si/SiO_2 (~ 10 Ωcm) substrates were utilized on which lithographically patterned Au source and drain electrodes were fabricated (L = 80 µm, W = 2.3 cm). This was followed by coating the perovskite layer in the same way as described above. The devices were then completed by coating a layer of Cytop to prevent any unwanted exposure of the perovskite samples to ambient condition. To avoid any degradation of the perovskite films and eliminate the features from water absorption the measurements were performed in a nitrogen environment with a humidity level of < 5%. Absorption spectra are obtained from Fast Fourier Transforms (FFT) of the time-resolved response (averaged over 4000 waveforms) from the perovskite film, the spectra were normalised to the response of a device without the perovskite layer.

Porosity Analysis of the Perovskite Films: To obtain the porosity of the perovskite films N_2 adsorption isotherms were measured on perovskite thin films fabricated on glass substrates (used for FET fabrication) at 77 K using a Micromeritics 3Flex instrument. Prior to the adsorption measurement, all samples were degassed at 100 °C for 1 h under high vacuum (10^{-6} mbar) to ensure that the pores of the perovskite films are as free as possible from any adsorbates or residual solvent without sample degradation. The isotherms were then measured without exposing them to ambient condition.

ESR measurement: All ESR spectra were taken in an Oxford Instruments ESR900 cryostat with a Bruker E500 X-band spectrometer. Measurements were recorded at a microwave frequency of approximately 9.4 GHz and a microwave power of 20 mW. The external field was modulated at a modulation frequency of ω_{mod} = 100 kHz to allow lock-in measurements and the modulation amplitude was B_{mod} = 1 G. These values were chosen such that the material was not saturated, i.e., the spins had enough time to relax between modulation cycles. (Equivalently, $\omega_{mod}B_{mod} << (\gamma T_1 T_2)^{-1}$ where T_1 and T_2 are the longitudinal and transverse spin relaxation times respectively). The number of spins is found by integration of the absorption spectrum (i.e., double integration of the ESR signal) using the following expression: $N_{spins} = \frac{k \times Area \times k_b T}{B_{mw} B_o S(S+1) \hbar \omega_{mw}}$ where k is a calibration factor for the spectrometer and sample position, B_0 is the Zeeman field, S is the spin (= 1/2 for electrons), ω_{mw} is the microwave frequency, k_b is the Boltzmann Constant and B_{mw} is the microwave field measured from the microwave power using the expression = (calibration constant) × $(Q \times P_{mw})^{1/2}$ where Q is the quality factor of the cavity and P_{mw} is the microwave power.

Photoluminescence Mapping: Photoluminescence measurements were performed using a confocal microscope (WITec Alpha RAS system). A fibre coupled 405-nm c.w. laser (Coherent CUBE) was focused on to the sample using 40x objective. The average power of the laser at its focal point was 0.5 μW. The photoluminescence of the sample was collected in the reflection geometry from the same objective while the excitation laser beam from the reflection is blocked using a 415 nm long-pass filter. The sample was mounted on an XYZ translation stage (piezo-electric) and raster scanned in 1 μm steps to collect the PL locally. Au-coated tungsten tips (having magnetic base) were used to contact the source and drain electrodes. The source-drain bias is applied using Keithley 2400 source meter. The collected PL spectrum was measured using calibrated Si-CCD array detector (Andor iDus BR-DD) fitted to a monochromator. All movements of the stage were automated and controlled by WITec ScanCtr spectroscopy Plus software. All photoluminescence spectra were performed in a N_2 atmosphere and averaged 10 times during the acquisition process. The measurements were repeated on three devices for consistency.

Figures:

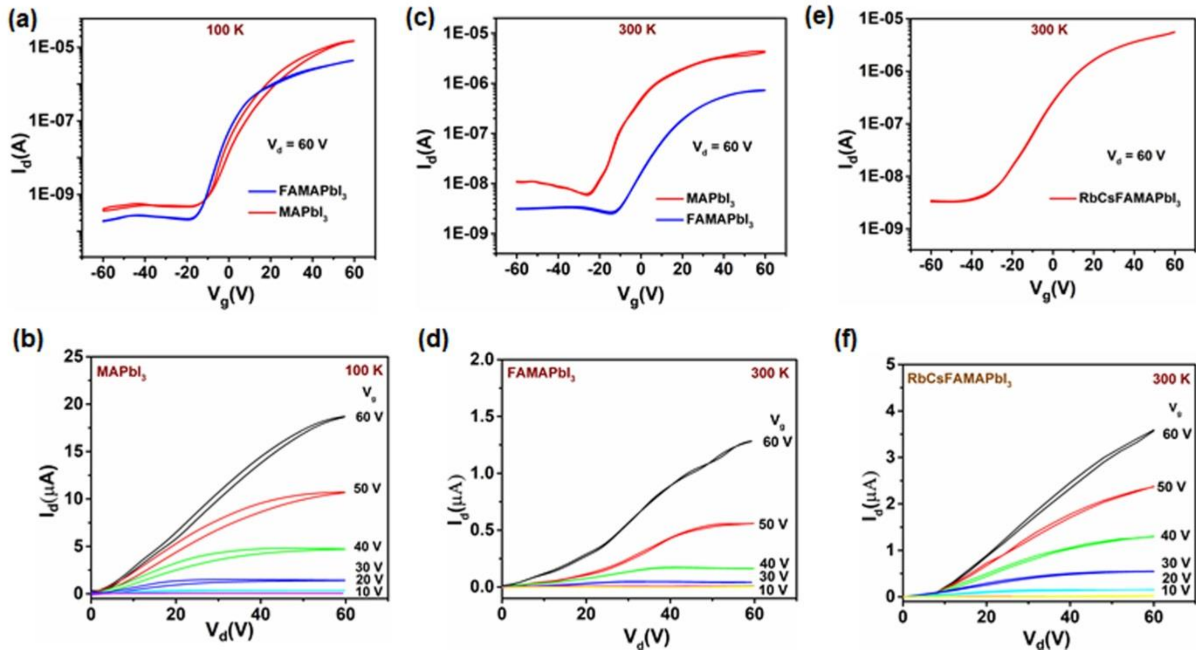

Figure 1: Top-gate perovskite FETs fabricated by the anti-solvent method - Effect of channel length and cation composition. (a) Transfer characteristics measured at 100 K on top-gate, bottom-contact perovskite FET fabricated from $MAPbI_3$ (red) and $FAMAPbI_3$ (blue) with L = 100 µm, W = 1mm; (b) Output characteristics measured on the same $MAPbI_3$ FET depicting a decrease in hysteresis compared to devices fabricated with L = 20 µm, W = 1mm (**Figure S1a** and **S2a**). Transfer characteristics measured at 300 K on perovskite FET (L = 100 µm, W = 1mm) fabricated from (c) $MAPbI_3$ (red), $FAMAPbI_3$ (blue). (d) Corresponding output characteristics measured on $FAMAPbI_3$ perovskite FETs with L = 100 µm, W = 1mm (e) Enhancement in the ON current in the transfer characteristics for FETs (L = 100 µm, W = 1mm) fabricated with $RbCsFAMAPbI_3$, the corresponding output characteristics (f) exhibits low hysteresis, but still some suppression of the current at small drain voltages indicating significant contact resistance.

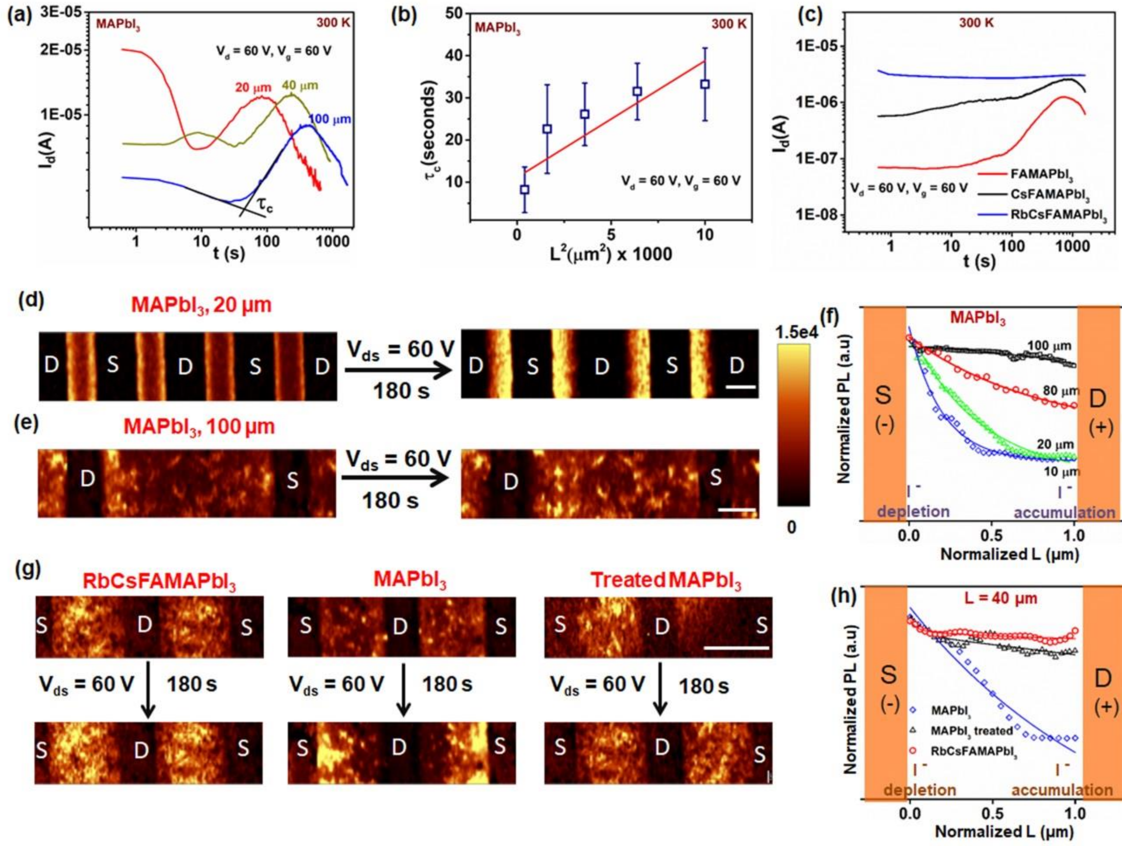

Figure 2: Measurements of lateral ion migration as a function of composition. (a) Temporal variation of I_{ds}, when a top gate $MAPbI_3$ transistor fabricated with different L is operated in trans-diode mode $V_d = V_g = 60$ V. (b) Plot of τ_c with L^2 indicating a typical time of flight behaviour. (c) Similar temporal variation of the I_{ds} measurement performed on top gate FETs (L = 100 µm, W = 1mm) fabricated with $FAMAPbI_3$, $CsFAMAPbI_3$ and $RbCsFAMAPbI_3$ perovskite layers. PL mapping performed on lateral channels of $MAPbI_3$ devices fabricated with different channel lengths (d) 20 µm, (e) 100 µm before and after application of a source-drain voltage of 60 V for 180 seconds. (f) Line profile of the PL along the channel in $MAPbI_3$ devices with different channel length. Lateral PL mapping measured on (g) $RbCsFAMAPbI_3$, $MAPbI_3$, Methyl Acetate (Lewis Base) treated $MAPbI_3$ devices fabricated with L = 40 µm. (h) Corresponding PL profiles obtained from the lateral cross-section of the different materials in (g) for a channel length of 40 µm. Scale bar in (d), (e) and (g) are 20 µm, 20 µm and 40 µm respectively.

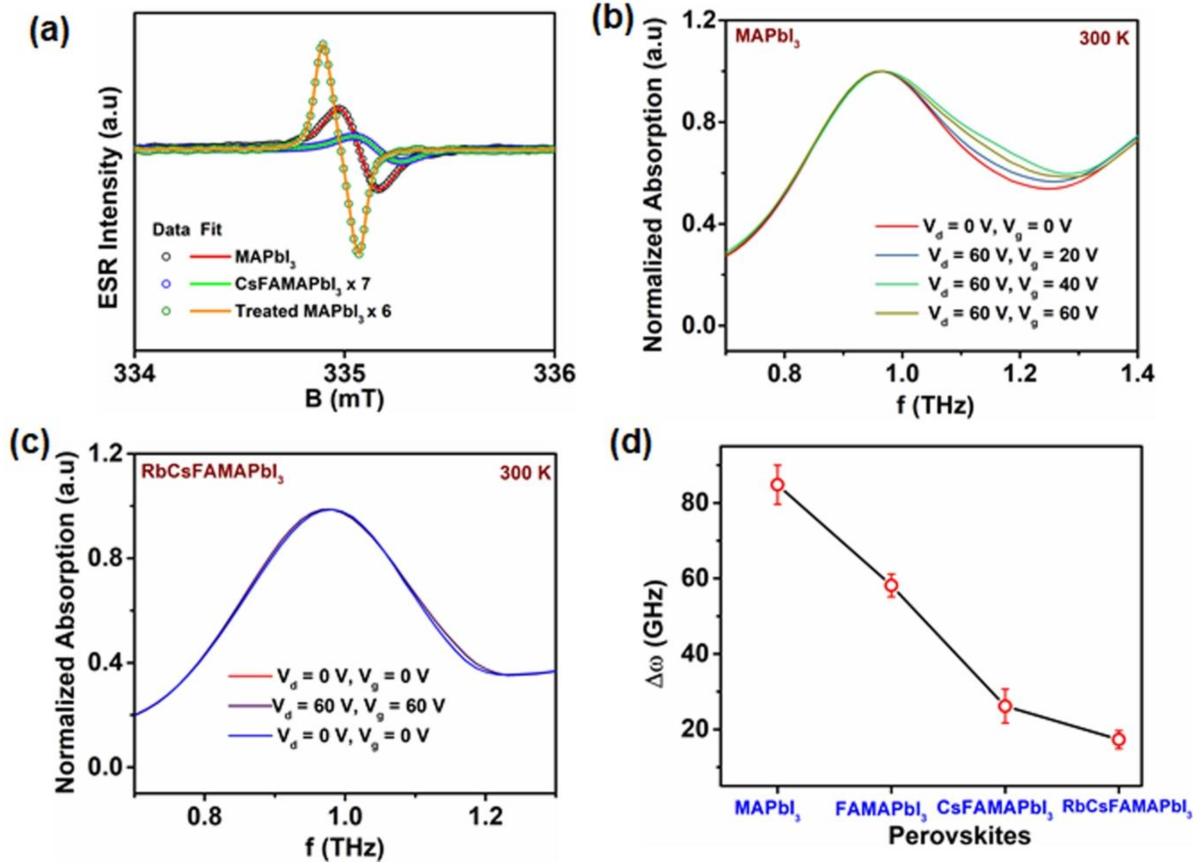

Figure 3: Spectroscopic characterization of defect states. (a) Derivative ESR spectra data (scatter) and best fits (line) measurement at 40 K performed on different perovskite samples. (b) Plot of the bias induced broadening of the first phonon peak around 1 THz in different perovskite materials. Bias-induced broadening is estimated from the difference in the FWHM for THz absorption spectra measured at $V_d = V_g = 0$ V and $V_d = V_g = 60$ V after a Gaussian fit. Representative THz absorption spectra measured on a bottom contact bottom gate transistor (L = 80 µm, W = 19.5 cm) fabricated using (c) $MAPbI_3$ (d) $RbCsFAMAPbI_3$ perovskite under different biasing conditions illustrating the broadening of the phonon mode.

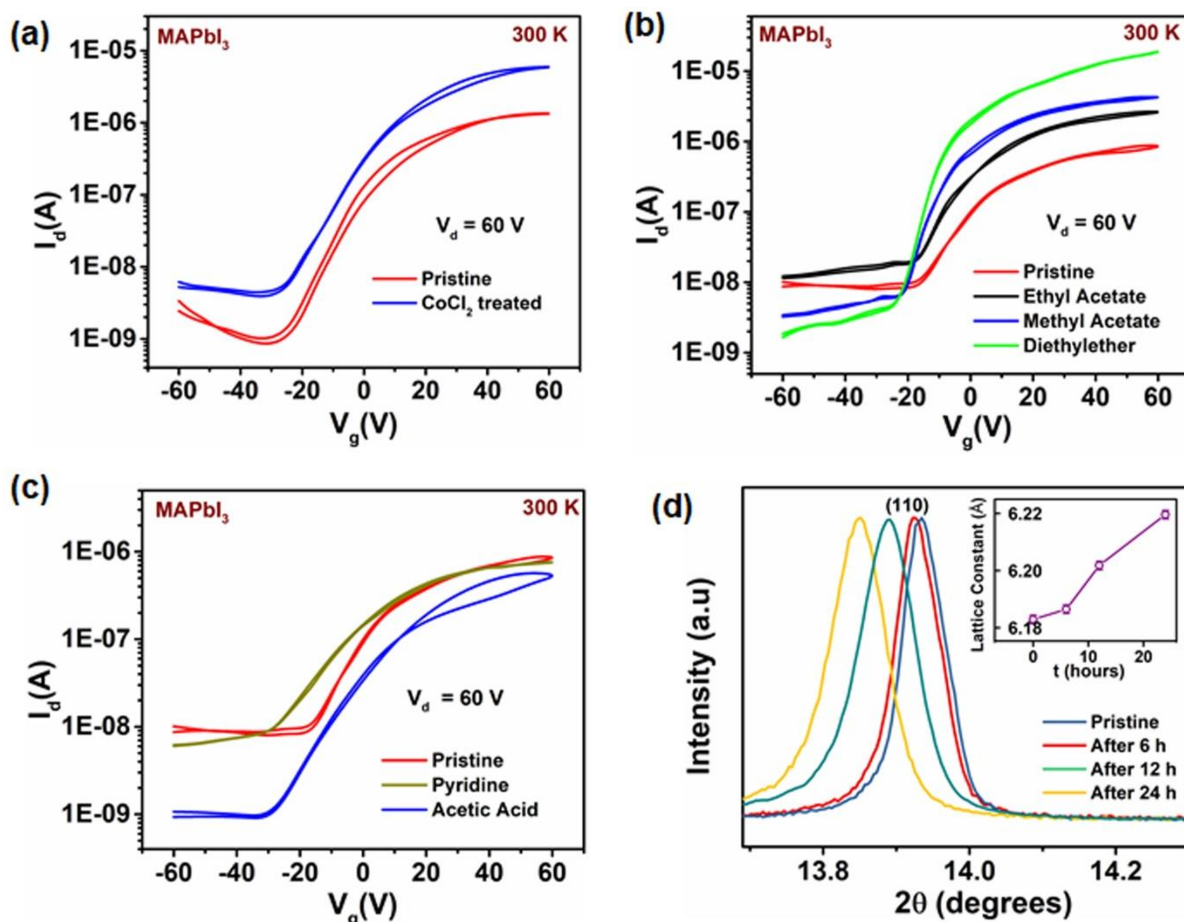

Figure 4: Enhancement of $MAPbI_3$ transistor performance with positive azeotrope, Lewis base solvent treatments. Variation in the transfer characteristics of $MAPbI_3$ perovskite FETs (L = 100 µm, W = 1 mm) (a) when exposed to a $CoCl_2$ desiccant layer. Also shown are treatments with a different class of orthogonal solvents: (b) Lewis bases - ethylacetate, methylacetate and diethyl ether, which also forms a low boiling azeotropic mixture with water; (c) Lewis bases, such as pyridine and acetic acid, which do not form a low boiling azeotropic mixture with water. (d) Shift in the XRD peak corresponding to (110) depicting the increase in lattice size upon treatment of $MAPbI_3$ films with methyl acetate solvent. Diethyl ether was avoided due to its low boiling point.

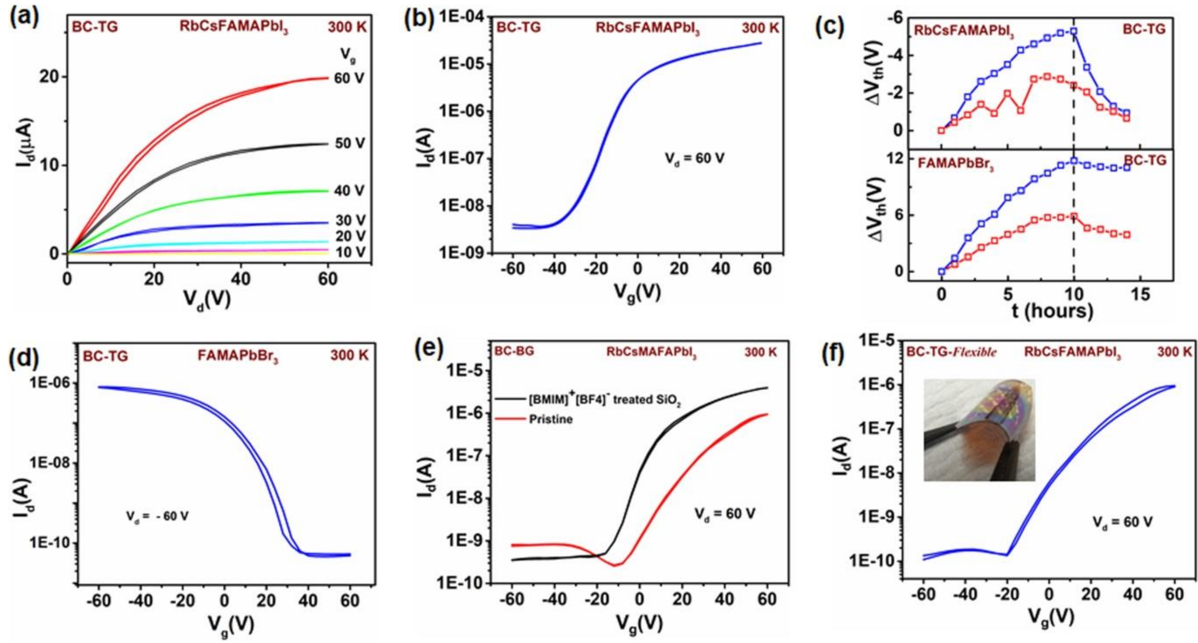

Figure 5: Performance of optimized p-type and n-type, top-gate and bottom-gate multiple cation perovskite FETs (a) Room temperature output and (b) transfer characteristics of bottom-contact top-gate (BC-TG) FETs (L = 100 µm, W = 1 mm) fabricated from diethyl ether treated $RbCsFAMAPbI_3$. (c) Comparison of voltage stress stability measured on bottom-contact top-gate (BC-TG) FETs fabricated from pristine (blue) and diethyl ether treated (red) perovskite layers of $RbCsFAMAPbI_3$ (top panel) and pristine (blue) as well as 1,3,5 tri-bromobenzene treated (blue) perovskite layer of $FAMAPbBr_3$ (bottom panel). (d) Transfer characteristics depicting optimized p-type bottom contact top gate perovskite transistor (BC-TG) FETs (L = 100 µm, W = 1 mm) fabricated from 1,3,5 tri-bromobenzene solvent treated $FAMAPbBr_3$ perovskite layer. (e) Room temperature transfer characteristics measured on bottom-contact, bottom-gate (BC-BG) $RbCsFAMAPbI_3$ based perovskite FETs (L = 100 µm, W = 1 mm) fabricated on ionic liquid $[BMIM]^+$ $[BF_4]^-$ treated SiO_2 interface (black) and pristine SiO_2 interface (red). (f) Bottom-contact top-gate (BC-TG) flexible perovskite FETs (L = 100 µm, W = 1 mm) fabricated with diethylether treated $RbCsFAMAPbI_3$. Photo credit: Satyaprasad P Senanayak, University of Cambridge,UK.

Contributions:

SPS performed the experiments on FET, fabricated the devices and samples for different experiments and wrote the manuscript with inputs from HS on the manuscript, data analysis and design. MAJ assisted SPS in the preparation of mixed perovskite samples and also performed the PDS measurements. RC performed the EPR measurements. VSK and HEB performed the THz measurements and DAR provided inputs on the measurement. RS and SPS performed the PL mapping measurements. TT and DFJ contributed in the N_2 adsorption isotherm measurements. NG and PD synthesized the methylammonium iodide precursor. DDN and SPS performed squid measurements. JW assisted SPS in the initial measurements of perovskite samples. GS grew the SAM layers on the Si/SiO_2 substrates. RHF and HS supervised the work. All authors discussed the results and revised the manuscript.

Acknowledgements

SPS acknowledges Dr. Cheng Liu for useful discussion in SQUID measurements. SPS and RS acknowledges funding from the Royal Society London for the Newton Fellowship. We acknowledge funding from the EPSRC through program grants EP/M005143/1, EP/P03148X/1 and EP/P021859/1. M.A.-J. thanks Cambridge Materials Limited for funding and technical support. G.S. acknowledges postdoctoral fellowship support from The Leverhulme Trust (Early Career Fellowship supported by the Isaac Newton Trust).The authors are grateful for funding from ERC Synergy Grand SC2 (No. 610115). D.F.-J. thanks the Royal Society for funding through a University Research Fellowship.

Conflict of Interest

The authors declare no competing interests

Data availability: All data needed to evaluate the conclusions in the paper are present in the paper and/or the Supplementary Materials. Additional data available from authors upon reasonable request.

References:

1. Nayak, P.K., Mahesh, S., Snaith, H.J. & Cahen, D. Photovoltaic solar cell technologies: analysing the state of the art. *Nature Reviews Materials* **4**, 269-285 (2019).
2. Zhao, B. et al. High-efficiency perovskite–polymer bulk heterostructure light-emitting diodes. *Nature Photonics* **12**, 783-789 (2018).
3. Stranks, S.D. & Snaith, H.J. Metal-halide perovskites for photovoltaic and light-emitting devices. *Nature Nanotechnology* **10**, 391 (2015).
4. Stranks, S.D. et al. Electron-Hole Diffusion Lengths Exceeding 1 Micrometer in an Organometal Trihalide Perovskite Absorber. *Science* **342**, 341-344 (2013).
5. Miyata, A. et al. Direct measurement of the exciton binding energy and effective masses for charge carriers in organic–inorganic tri-halide perovskites. *Nature Physics* **11**, 582 (2015).
6. Wang, T. et al. Indirect to direct bandgap transition in methylammonium lead halide perovskite. *Energy & Environmental Science* **10**, 509-515 (2017).
7. Christians, J.A. et al. Tailored interfaces of unencapsulated perovskite solar cells for >1,000 hour operational stability. *Nature Energy* **3**, 68-74 (2018).
8. Hou, Y. et al. A generic interface to reduce the efficiency-stability-cost gap of perovskite solar cells. *Science* **358**, 1192-1197 (2017).
9. Zhu, H. et al. Perovskite and Conjugated Polymer Wrapped Semiconducting Carbon Nanotube Hybrid Films for High-Performance Transistors and Phototransistors. *ACS Nano* **13**, 3971-3981 (2019).
10. Aleshin, A.N., Shcherbakov, I.P., Gushchina, E.V., Matyushkin, L.B. & Moshnikov, V.A. Solution-processed field-effect transistors based on polyfluorene –cesium lead halide nanocrystals composite films with small hysteresis of output and transfer characteristics. *Organic Electronics* **50**, 213-219 (2017).
11. Zhu, L. et al. Synthesis of ultrathin two-dimensional organic–inorganic hybrid perovskite nanosheets for polymer field-effect transistors. *Journal of Materials Chemistry C* **6**, 3945-3950 (2018).
12. Arora, N. et al. Perovskite solar cells with CuSCN hole extraction layers yield stabilized efficiencies greater than 20%. *Science* **358**, 768-771 (2017).
13. You, J. et al. Improved air stability of perovskite solar cells via solution-processed metal oxide transport layers. *Nature Nanotechnology* **11**, 75 (2015).
14. Saliba, M. et al. Incorporation of rubidium cations into perovskite solar cells improves photovoltaic performance. *Science*, aah5557 (2016).
15. Wang, Z. et al. Efficient ambient-air-stable solar cells with 2D–3D heterostructured butylammonium-caesium-formamidinium lead halide perovskites. *Nature Energy* **2**, 17135 (2017).
16. Tsai, H. et al. High-efficiency two-dimensional Ruddlesden–Popper perovskite solar cells. *Nature* **536**, 312 (2016).
17. Lin, K. et al. Perovskite light-emitting diodes with external quantum efficiency exceeding 20 per cent. *Nature* **562**, 245-248 (2018).
18. Jia, Y., Kerner, R.A., Grede, A.J., Rand, B.P. & Giebink, N.C. Continuous-wave lasing in an organic–inorganic lead halide perovskite semiconductor. *Nature Photonics* **11**, 784-788 (2017).
19. Chin, X.Y., Cortecchia, D., Yin, J., Bruno, A. & Soci, C. Lead iodide perovskite light-emitting field-effect transistor. *Nature Communications* **6**, 7383 (2015).
20. Li, F. et al. Ambipolar solution-processed hybrid perovskite phototransistors. *Nature Communications* **6**, 8238 (2015).
21. Mei, Y., Zhang, C., Vardeny, Z.V. & Jurchescu, O.D. Electrostatic gating of hybrid halide perovskite field-effect transistors: balanced ambipolar transport at room-temperature. *MRS Communications* **5**, 297-301 (2015).

22. Li, D. et al. Size-dependent phase transition in methylammonium lead iodide perovskite microplate crystals. *Nature Communications* **7**, 11330 (2016).
23. Labram, J.G. et al. Temperature-Dependent Polarization in Field-Effect Transport and Photovoltaic Measurements of Methylammonium Lead Iodide. *The Journal of Physical Chemistry Letters* **6**, 3565-3571 (2015).
24. Yu, W. et al. Single crystal hybrid perovskite field-effect transistors. *Nature Communications* **9**, 5354 (2018).
25. Senanayak, S.P. et al. Understanding charge transport in lead iodide perovskite thin-film field-effect transistors. *Science Advances* **3**, e1601935 (2017).
26. Lin, Y.-H., Pattanasattayavong, P. & Anthopoulos, T.D. Metal-Halide Perovskite Transistors for Printed Electronics: Challenges and Opportunities. *Advanced Materials* **29**, 1702838 (2017).
27. Saliba, M. et al. Cesium-containing triple cation perovskite solar cells: improved stability, reproducibility and high efficiency. *Energy & Environmental Science* **9**, 1989-1997 (2016).
28. Yusoff, A.R.b.M. et al. Ambipolar Triple Cation Perovskite Field Effect Transistors and Inverters. *Advanced Materials* **29**, 1602940 (2017).
29. Ndione, P.F., Li, Z. & Zhu, K. Effects of alloying on the optical properties of organic–inorganic lead halide perovskite thin films. *Journal of Materials Chemistry C* **4**, 7775-7782 (2016).
30. Herz, L.M. Charge-Carrier Mobilities in Metal Halide Perovskites: Fundamental Mechanisms and Limits. *ACS Energy Letters* **2**, 1539-1548 (2017).
31. Onoda-Yamamuro, N., Matsuo, T. & Suga, H. Dielectric study of CH3NH3PbX3 (X = Cl, Br, I). *Journal of Physics and Chemistry of Solids* **53**, 935-939 (1992).
32. Frost, J.M. et al. Atomistic Origins of High-Performance in Hybrid Halide Perovskite Solar Cells. *Nano Letters* **14**, 2584-2590 (2014).
33. Ma, F. et al. Stable α/δ phase junction of formamidinium lead iodide perovskites for enhanced near-infrared emission. *Chemical Science* **8**, 800-805 (2017).
34. Binek, A., Hanusch, F.C., Docampo, P. & Bein, T. Stabilization of the Trigonal High-Temperature Phase of Formamidinium Lead Iodide. *The Journal of Physical Chemistry Letters* **6**, 1249-1253 (2015).
35. Hu, Y., Aygüler, M.F., Petrus, M.L., Bein, T. & Docampo, P. Impact of Rubidium and Cesium Cations on the Moisture Stability of Multiple-Cation Mixed-Halide Perovskites. *ACS Energy Letters* **2**, 2212-2218 (2017).
36. Hu, Y. et al. Understanding the Role of Cesium and Rubidium Additives in Perovskite Solar Cells: Trap States, Charge Transport, and Recombination. *Advanced Energy Materials* **8**, 1703057 (2018).
37. Abdi-Jalebi, M. et al. Maximizing and stabilizing luminescence from halide perovskites with potassium passivation. *Nature* **555**, 497 (2018).
38. Besleaga, C. et al. Iodine Migration and Degradation of Perovskite Solar Cells Enhanced by Metallic Electrodes. *The Journal of Physical Chemistry Letters* **7**, 5168-5175 (2016).
39. Li, C. et al. Real-Time Observation of Iodide Ion Migration in Methylammonium Lead Halide Perovskites. *Small* **13**, 1701711 (2017).
40. Senocrate, A. et al. The Nature of Ion Conduction in Methylammonium Lead Iodide: A Multimethod Approach. *Angewandte Chemie International Edition* **56**, 7755-7759 (2017).
41. deQuilettes, D.W. et al. Photo-induced halide redistribution in organic–inorganic perovskite films. *Nature Communications* **7**, 11683 (2016).
42. Bollmann, W., Uvarov, N.F. & Hairetdinov, E.F. Estimation of point defect parameters of solids on the basis of a defect formation model of melting (II). Vacancy formation enthalpy in relation to the heat of fusion and the increase of volume due to melting. *Crystal Research and Technology* **24**, 421-435 (1989).

43. Shkrob, I.A. & Marin, T.W. Charge Trapping in Photovoltaically Active Perovskites and Related Halogenoplumbate Compounds. *The Journal of Physical Chemistry Letters* **5**, 1066-1071 (2014).
44. Colella, S. et al. Light-Induced Formation of Pb3+ Paramagnetic Species in Lead Halide Perovskites. *ACS Energy Letters* **3**, 1840-1847 (2018).
45. Sun, Q. et al. Highly Sensitive Terahertz Thin-Film Total Internal Reflection Spectroscopy Reveals in Situ Photoinduced Structural Changes in Methylammonium Lead Halide Perovskites. *The Journal of Physical Chemistry C* **122**, 17552-17558 (2018).
46. Leguy, A.M.A. et al. Dynamic disorder, phonon lifetimes, and the assignment of modes to the vibrational spectra of methylammonium lead halide perovskites. *Physical Chemistry Chemical Physics* **18**, 27051-27066 (2016).
47. Aschauer, U., Pfenninger, R., Selbach, S.M., Grande, T. & Spaldin, N.A. Strain-controlled oxygen vacancy formation and ordering in CaMnO${}_{3}$. *Physical Review B* **88**, 054111 (2013).
48. Saidaminov, M.I. et al. Suppression of atomic vacancies via incorporation of isovalent small ions to increase the stability of halide perovskite solar cells in ambient air. *Nature Energy* **3**, 648-654 (2018).
49. Bobbert, P.A., Sharma, A., Mathijssen, S.G.J., Kemerink, M. & de Leeuw, D.M. Operational Stability of Organic Field-Effect Transistors. *Advanced Materials* **24**, 1146-1158 (2012).
50. Aristidou, N. et al. Fast oxygen diffusion and iodide defects mediate oxygen-induced degradation of perovskite solar cells. *Nature Communications* **8**, 15218 (2017).
51. Nikolka, M. et al. High operational and environmental stability of high-mobility conjugated polymer field-effect transistors through the use of molecular additives. *Nature Materials* **16**, 356 (2016).
52. Ciccioli, A. & Latini, A. Thermodynamics and the Intrinsic Stability of Lead Halide Perovskites CH3NH3PbX3. *The Journal of Physical Chemistry Letters* **9**, 3756-3765 (2018).
53. Huang, J., Tan, S., Lund, P.D. & Zhou, H. Impact of H2O on organic–inorganic hybrid perovskite solar cells. *Energy & Environmental Science* **10**, 2284-2311 (2017).
54. Baikie, T. et al. Synthesis and crystal chemistry of the hybrid perovskite (CH3NH3)PbI3 for solid-state sensitised solar cell applications. *Journal of Materials Chemistry A* **1**, 5628-5641 (2013).
55. Nikolka, M. et al. Performance Improvements in Conjugated Polymer Devices by Removal of Water-Induced Traps. *Advanced Materials* **30**, 1801874 (2018).
56. Oxtoby, D.W.G., H.P., Butler, L. J Principles of Modern Chemistry, Vol. 4th Edition. (Brooks Cole., 2015).
57. Horsley, L.H. Azeotropic Data—III, Vol. 116. (AMERICAN CHEMICAL SOCIETY, 1973).
58. Shi, D. et al. Low trap-state density and long carrier diffusion in organolead trihalide perovskite single crystals. *Science* **347**, 519-522 (2015).
59. Abdi-Jalebi, M. et al. Impact of Monovalent Cation Halide Additives on the Structural and Optoelectronic Properties of CH3NH3PbI3 Perovskite. *Advanced Energy Materials* **6**, 1502472 (2016).
60. Fassl, P. et al. Fractional deviations in precursor stoichiometry dictate the properties, performance and stability of perovskite photovoltaic devices. *Energy & Environmental Science* **11**, 3380-3391 (2018).